Check for updates

ADVANCED ENERGY MATERIALS
www.advenergymat.de

Efficiency Boost in All-Small-Molecule Organic Solar Cells: Insights from the Re-Ordering Kinetics

Xiaokang Sun, Jie Lv, Fei Wang, Chenyang Zhang, Liangxiang Zhu, Guangye Zhang, Tongle Xu, Zhenghui Luo, Haoran Lin, Xiaoping Ouyang, Chunming Yang, Chuluo Yang, Gang Li,* and Hanlin Hu**

Achieving high-performance in all-small-molecule organic solar cells (ASM-OSCs) significantly relies on precise nanoscale phase separation through domain size manipulation in the active layer. Nonetheless, for ASM-OSC systems, forging a clear connection between the tuning of domain size and the intricacies of phase separation proves to be a formidable challenge. This study investigates the intricate interplay between domain size adjustment and the creation of optimal phase separation morphology, crucial for ASM-OSCs' performance. It is demonstrated that exceptional phase separation in ASM-OSCs' active layer is achieved by meticulously controlling the continuity and uniformity of domains via re-packing process. A series of halogen-substituted solvents (Fluorobenzene, Chlorobenzene, Bromobenzene, and Iodobenzene) is adopted to tune the re-packing kinetics, the ASM-OSCs treated with CB exhibited an impressive 16.2% power conversion efficiency (PCE). The PCE enhancement can be attributed to the gradual crystallization process, promoting a smoothly interconnected and uniformly distributed domain size. This, in turn, leads to a favorable phase separation morphology, enhanced charge transfer, extended carrier lifetime, and consequently, reduced recombination of free charges. The findings emphasize the pivotal role of re-packing kinetics in achieving optimal phase separation in ASM-OSCs, offering valuable insights for designing high-performance ASM-OSCs fabrication strategies.

1. Introduction

Organic solar cells (OSCs), as a prominent avenue in the realm of clean energy development and utilization, derive their photoactive layer materials from abundant sources and offer an environmentally benign decomposition process (the materials primarily consist of elements such as C, H, O, N, and S). This abundance of source materials bestows boundless opportunities for conceiving and advancing novel photovoltaic materials for the active layer. Furthermore, the exceptional practical benefits of OSCs extend to a wide array of applications, including semitransparent devices, flexible panels, indoor lighting, Internet of Things, and wearables, thus garnering considerable attention.[1–4] Amid the advancement of exceptional nonfullerene acceptors like Y6 and its derivatives, coupled with advancements in device technology, the power conversion efficiency (PCE) of OSCs founded on polymers as donors has surpassed the 19% milestone.[5–9] Furthermore,

X. Sun, J. Lv, F. Wang, C. Zhang, H. Lin, H. Hu
Hoffmann Institute of Advanced Materials
Shenzhen Polytechnic University
7098 Liuxian Boulevard, Shenzhen 518055, P. R. China
E-mail: hanlinhu@szpu.edu.cn

X. Sun, X. Ouyang
School of Materials Science and Engineering
Xiangtan University
Xiangtan 411105, P. R. China

J. Lv
Shenzhen Institutes of Advanced Technology
Chinese Academy of Sciences
Shenzhen 518055, P. R. China

J. Lv
University of Chinese Academy of Sciences
Beijing 100049, P. R. China

C. Zhang
Institute of Flexible Electronics (IFE)
Northwestern Polytechnical University (NPU)
Research & Development Institute of Northwestern Polytechnical University in Shenzhen
Xi'an 710072, P. R. China

L. Zhu, G. Zhang
College of New Materials and New Energies
Shenzhen Technology University
Shenzhen 518118, P. R. China

T. Xu, Z. Luo, C. Yang
Shanghai Synchrotron Radiation Facility
Shanghai Advanced Research Institute
Chinese Academy of Sciences
Shanghai 201204, P. R. China
E-mail: yangchunming@zjlab.org.cn

The ORCID identification number(s) for the author(s) of this article can be found under https://doi.org/10.1002/aenm.202302731

DOI: 10.1002/aenm.202302731

 © 2023 Wiley-VCH GmbH

the PCE of all-small-molecule OSCs (ASM-OSCs), which consist of small molecule donors and small molecule acceptors, has crossed the 17% threshold.[10–11] In contrast to polymer-based OSCs, small molecules possess promising application potential and the capacity for large-scale commercial manufacturing, thanks to their distinct molecular structure, facile purification, tunable structure, and device reproducibility.[12–14] Nevertheless, the PCE of ASM-OSCs still trails behind that of polymer-based OSCs. Furthermore, due to the limited advancement of small molecule donor materials, controlling the domain size of the donor/acceptor mixed morphology within the active layer of ASM-OSCs heterojunction (BHJ) remains a challenge in the pursuit of high PCE.

Broadly speaking, attaining an exceptional BHJ morphology within the ASM-OSCs system serves as the cornerstone for enhancing its performance. This excellent active layer morphology should encompass a favorable phase separation, ordered molecular stacking, and a well-suited hierarchical structure.[15–16] However, owing to the restricted conjugation length and inherent crystal self-aggregation tendencies of small molecule materials, this frequently results in an excessive phase separation morphology and domain size within the active layer. These factors impede exciton dissociation and charge transfer, ultimately culminating in diminished short-circuit current density (J_{SC}) and fill factor (*FF*) in ASM-OSCs. Based on the ASM-OSCs systems currently documented, enhancing the structural characteristics of small molecule donor materials can ameliorate the phase separation structure of ASM-OSCs, yielding an appropriate domain size. For example, Yang et al. reported that small molecule donor TB-F was obtained by asymmetric thiobenzene and phenyl side chain modification of the BDT core on the small molecule donor BTR-Cl, the blend film based on TB-F:L8-BO exhibits significant phase separation and has coarse and long fiber domain sizes, constructing a good continuous interpenetrating morphology, thereby improving the J_{SC} and *FF* of the corresponding devices.[17] Wei et al. obtained M-PhS by moving the alkyl thiolation side chain from the para- to meta-positions of the small molecule donor ZR1 molecular backbone, enhancing the surface tension and molecular planarity of the molecule, and blending with BTP-eC9 achieved a multi-length scale domain and highly ordered morphology, enhanced interaction with acceptor molecules, and achieved J_{SC} of 25.4 mA cm^{-2} and *FF* of 75.6%.[14] Ge et al. applied asymmetric modulation to the end groups of the small molecule donor by utilizing the end groups of 2-ethylhexyl cyanoacetate (CA) and 2-ethylhexyl rhodanni ne (Reh) to create an asymmetric donor labeled as SM-CA-Reh (influenced by Reh single substitution). When coupled with acceptor N3, this design facilitated appropriate phase separation and domain size of the molecules, leading to an impressive FF of 77.5%.[18] Furthermore, by incorporating a well-suited third component into the small molecule systems, the domain size of the BHJ morphology in ASM-OSCs can also be enhanced. For instance, Hou et al., utilizing the small molecule system of B1:BO-4Cl, integrated a 0.5% weight acceptor BO-2Cl to substitute for BO-4Cl. This led to the development of a nanoscale double continuous interpenetrating network, featuring a hierarchical branching structure. This innovative approach amplified the charge transfer performance of the domain size, culminating in a remarkable FF of 78%.[19] Lu et al. incorporated a small quantity of $PC_{71}BM$, known for its proficient electron transport capabilities, to enhance the phase separation within the BTR-Cl:Y6 blend film. This strategic inclusion led to an expansion in the domain size structure, ultimately culminating in an impressive FF of 77%.[20] In summary, the regulation of domain size in ASM-OSCs holds pivotal significance in enhancing charge transport performance and PCE. However, there is a dearth of comprehensive exploration into the construction methodology of ASM-OSCs domain size as well as the intricate interplay between domain size and performance.

In this work, we selected the T6:N3 as the research system and employed the widely utilized solvent vapor annealing (SVA) process in ASM-OSCs to manipulate the morphology in the blend film (in **Figure 1**a),[21–22] and a comprehensive investigation was undertaken to systematically examine the effect on domain size and crystallinity in blend films using solvents substituted with distinct halogens (Fluorobenzene (FB), Chlorobenzene (CB), Bromobenzene (BB), and Iodobenzene (IB)). In addition, in situ UV–vis absorption spectroscopy was utilized to study the evolution kinetics of aggregation and crystallization in blend films during the SVA process. To our astonishment, we discovered that halogen elements exert a significant influence on the morphology of blend films during the re-ordering process. Figure 1b illustrates a schematic representation of the domain size and morphology distribution within the thin films treated with FB, CB, BB, and IB: Specifically, the T6:N3 thin film treated with CB exhibited a minimal domain size with relatively low crystallinity, remarkable continuity, and even distribution. This led to the attainment of a maximum PCE of 16.2% and a FF of 74.3%. On the other hand, films treated with BB and IB both displayed intermediate domain sizes primarily, alongside a mutual presence of small domain sizes, resulting in identical PCEs of 15.3% and 15.2%, respectively, accompanied by comparable FF values. In contrast, the film treated with FB underwent the rapid expansion of non-uniform domain sizes, which, in turn, triggered pronounced charge recombination, culminating in a lower PCE of 14.8% and an FF of 69.1%. Our results fully demonstrate that fine regulation of the domain size of ASM-OSCs can reduce charge recombination and enhance charge transfer, which further paves the way for unleashing the efficiency potential of ASM-OSCs.

2. Results and Discussion

To obtain a comprehensive understanding of the process of SVA and the influence of different solvents, in situ UV–vis spectroscopy was employed to observe translational movement and

C. Yang
Shenzhen Key Laboratory of New Information Display and Storage Materials
College of Materials Science and Engineering
Shenzhen University
Shenzhen 518060, P. R. China
G. Li
Department of Electronic and Information Engineering
Research Institute for Smart Energy (RISE)
The Hong Kong Polytechnic University
Kowloon, Hong Kong P. R. China
E-mail: gang.w.li@polyu.edu.hk

© 2023 Wiley-VCH GmbH

16146840, 0, Downloaded from https://onlinelibrary.wiley.com/doi/10.1002/aenm.202302731 by Shenzhen Polytechnic, Wiley Online Library on [22/11/2023]. See the Terms and Conditions (https://onlinelibrary.wiley.com/terms-and-conditions) on Wiley Online Library for rules of use; OA articles are governed by the applicable Creative Commons License

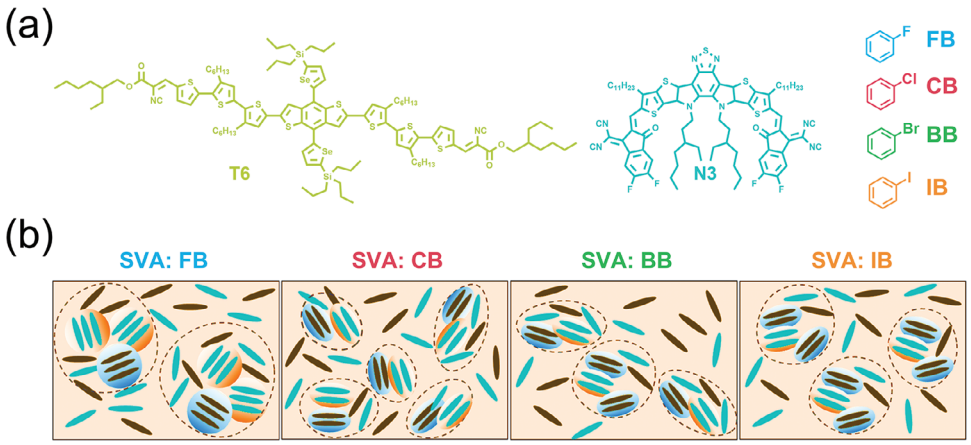

Figure 1. a) Chemical structures of T6 and N3. b) Schematics of the film morphology of T6: N3 blends film with SVA processing under different solvent conditions.

reconfiguration of the molecular orientation, which can reflect the kinetics of crystallinity and domain size in thin films.

We monitored the SVA process under different solvent conditions via in situ UV–vis absorption and explored the effect of different solvents on the morphology modulation combined with other characterizations. **Figure 2**a–d presents contour maps during the SVA process under different solvent conditions. It becomes evident that the absorption characteristics of films treated with various solvents exhibit a remarkably consistent evolution, accompanied by a substantial enhancement in absorption. However, apart from the CB-treated film, all films under other solvent conditions rapidly transitioned to the absorption enhancement stage, evidenced by substantial absorption changes in both T6 and N3 (Figure 2a–d and Figure S1, Supporting Information), which corresponds to the rapid transformation of the morphology in the blend film over a short period. This may have a serious impact on the SVA process due to the different vapor pressures of different solvents and the solubility of materials.[22–24] Therefore, in order to understand the impact of the property of solvents on the blend film during the SVA process, we estimated the saturated vapor pressure of four solvents (FB, CB, BB, and IB) through calculations and tested the solubility of four solvents for T6 and N3 (Tables S1 and Tables S2, Supporting Information). We found that FB has the lowest solubility for T6 and N3 among all solvents, while BB and IB have the highest solubility, with CB in the middle. By analyzing the relationship between the contour map of in situ absorption and solubility (Figure 2a-d; Figure S1, Supporting Information), we found that the morphology of the blend films could be rapidly transitioned to the absorption enhancement stage under the treatment of low saturated vapor pressure and high solubility of BB and IB. Meanwhile, a rapid absorption enhancement stage was also observed under FB treatment with high saturated vapor pressure and low solubility. We speculate that this is most likely due to the dominant role of the high saturated vapor pressure of FB and the auxiliary role of low solubility. However, BB and IB also contribute to the absorption transition of the films at low saturated vapor pressure due to their high solubility. Thus, the solvent CB balances the relationship between saturation vapor pressure and solubility and ultimately exhibits a uniform and slowly varying absorption enhancement process in the contour plots, which may be a factor in achieving optimal film morphology.

Integrated with morphological characterization, we explored the impact of distinct SVA processes on the morphology modulation. The surface morphology of the blend film was characterized using Atomic Force Microscope (AFM) and Transmission Electron Microscope (TEM) measurements, as shown in Figure 2e–l. As the AFM images demonstrated, by carefully observing AFM images and local magnified images, it can be found that the CB treated film formed a small and uniform continuous surface morphology, obtaining a lower root-mean-square roughness (R_q) value of 1.42 nm, a smaller value of R_q is beneficial for improving interface stability and reducing interface resistance.[25] In the BB and IB treated films, finer granular structures were found and larger uneven surface morphology was formed, resulting in slightly increased R_q of 1.49 and 1.56 nm, respectively. However, the FB treated film forms a surface morphology with larger particle size structures, resulting in a maximum R_q of 2.71 nm, and this uneven large particle size structure often leads to poor charge recombination. Based on TEM images, it is obvious that the FB treated films show large and discontinuous phase separation morphology and domain size structure, which is not conducive to exciton separation at the donor-acceptor interface (Figure 2i). The CB-treated film exhibits a fibrous phase separation morphology, and the small domain size structure constitutes a good interpenetrating network morphology in Figure 2j, this provides an ideal channel for the dissociation of excitons and charge transfer, which is beneficial for reducing charge recombination.[5] The films treated with BB and IB exhibit larger domain size structures and similar phase separation morphology. The vertical analysis under different solvent treatment conditions is beneficial for further understanding the relationship between photovoltaic performance and morphology. Therefore, we investigated the vertical segregation of T6:N3 thin films under different solvent conditions using film-depth-dependent light absorption spectroscopy (FLAS). Figure 2d and Figure S2e–h (Supporting Information) illustrate the component distribution and contour maps of the exciton generation rate in T6:N3 films. In the SVA-treated films, the interpenetrating part is predominantly located in the middle region, while the main donor-rich distribution tends to approach

© 2023 Wiley-VCH GmbH

16146840, 0, Downloaded from https://onlinelibrary.wiley.com/doi/10.1002/aenm.202302731 by Shenzhen Polytechnic, Wiley Online Library on [22/11/2023]. See the Terms and Conditions (https://onlinelibrary.wiley.com/terms-and-conditions) on Wiley Online Library for rules of use; OA articles are governed by the applicable Creative Commons License

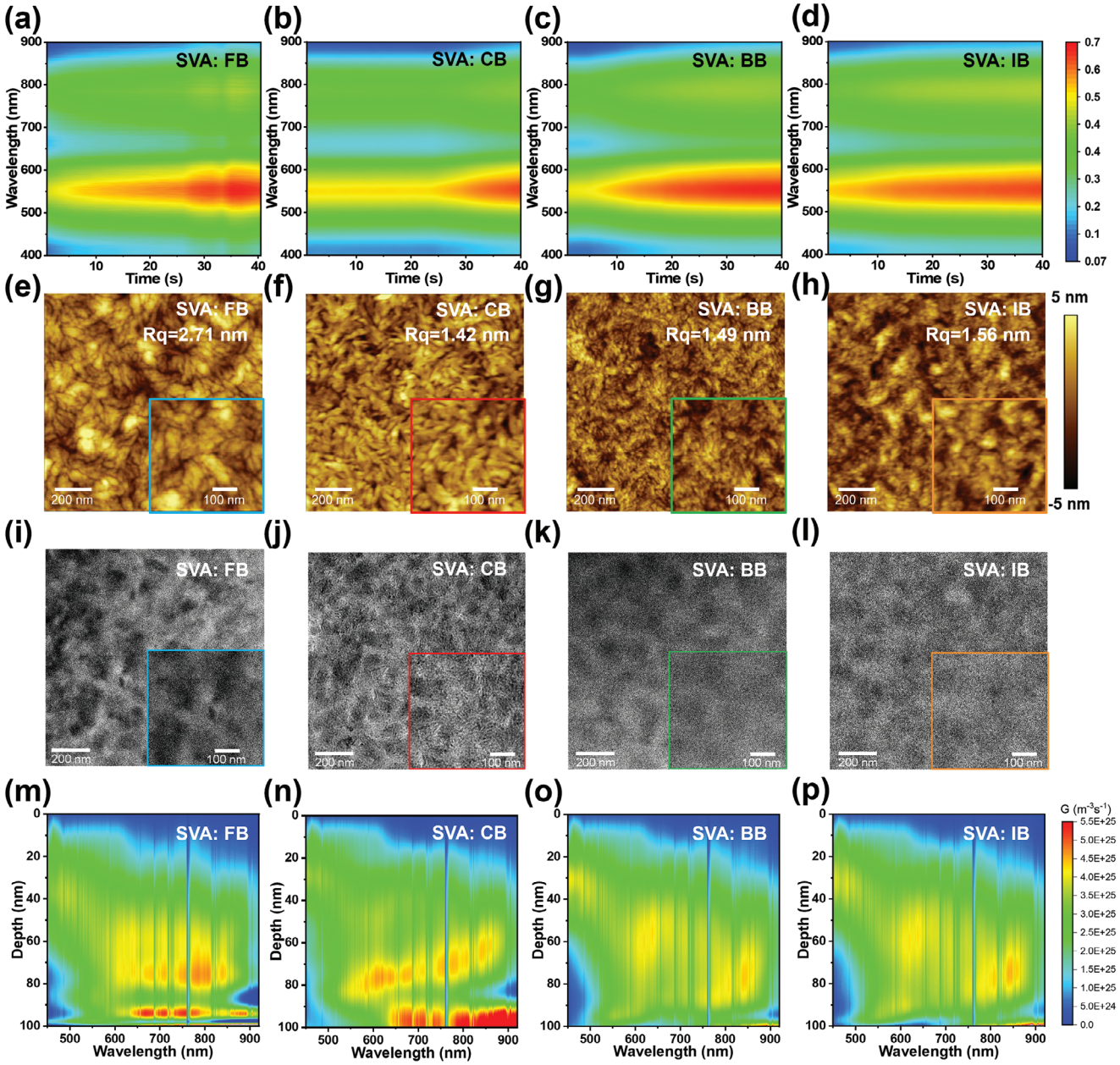

Figure 2. a–d) Contour map of T6: N3 films treated with FB, CB, BB, and IB, respectively. e–h) AFM height images of T6: N3 films under different treated conditions. i–l) TEM images under different treated conditions. m–p) The contours of exciton generation rate of T6: N3 films under different treated conditions.

the top and bottom regions. Moreover, for the CB-treated film, the T6 enrichment at the bottom was more significant than that in other solvent-treated films, which are more beneficial to enhancing charge transfer and reducing surface recombination.[25–26] However, the CB-treated film exhibits a more homogeneous distribution of the acceptor and donor in the middle region, indicating a better phase separation in the vertical film thickness direction. Figure S2 (Supporting Information) displays the absorption spectra and exciton generation rates at various depths of T6:N3 films under different conditions. It can be observed that when the film depth is in the range of 15 to 60 nm, the exciton generation rates (Gs) (Figure S2I, Supporting Information) of the BB and IB-treated films are higher than those of the FB and CB-treated films. This observation explains the larger J_{SC} observed in the IB-treated devices.

To further explore the impact of SVA on blend films, we examined the prolonged evolution (200 s) of the SVA process under CB conditions, as illustrated in **Figure 3**. The alterations in absorption intensity and peak position can be clearly tracked throughout the SVA process. From Figure 3a, it can be observed that the absorption intensity gradually increases, and the absorption position of N3 exhibits a significant redshift. It indicates an

© 2023 Wiley-VCH GmbH

16146840, 0, Downloaded from https://onlinelibrary.wiley.com/doi/10.1002/aenm.202302731 by Shenzhen Polytechnic, Wiley Online Library on [22/11/2023]. See the Terms and Conditions (https://onlinelibrary.wiley.com/terms-and-conditions) on Wiley Online Library for rules of use; OA articles are governed by the applicable Creative Commons License

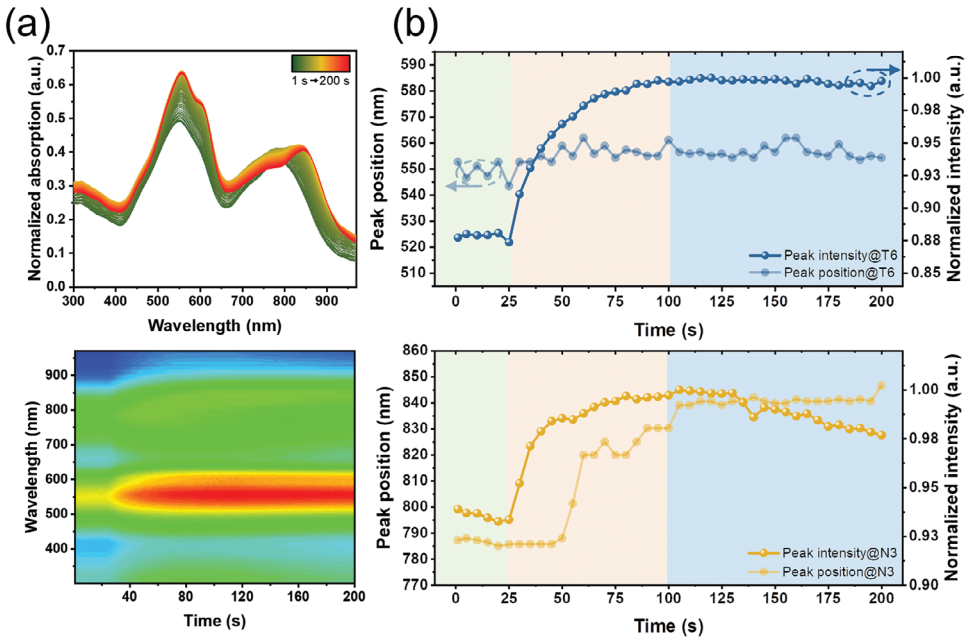

Figure 3. a) In situ UV–vis absorption spectra and contour map during SVA with CB. b) Time evolution of normalized absorption at 570 nm (T6) and 840 nm (N3) during SVA with CB.

enhancement in crystallinity within the blend film and the noticeable aggregation of N3 molecules. Additionally, during the SVA process, a gradual enhancement of *J*-aggregation for T6 is observed, which is beneficial for hole transport.[22] The time evolution of normalized absorption for T6 and N3 was extracted from the in situ UV–vis absorption spectra, revealing the aggregation evolution during the SVA process of the T6:N3 blend. As shown in Figure 3b, the SVA process can be divided into three stages. In the 1st stage (colored green), no significant changes are observed. The limited molecular movement results in minimal changes within the blend film. In the 2nd stage (colored yellow), a significant increase in intensity is observed, accompanied by a red-shift in both absorption peaks. Specifically, for the absorption peak of T6, only a slight red-shift occurs compared to the as-cast film, which indicates a slight increase in the planarization of the T6 backbone.[27–28] In contrast, the peak positions of N3 exhibit a significant red-shift from 788 to 840 nm. This pronounced red-shift can be attributed to the intercalation of N3 molecules into the T6 matrix, which creates charge-transfer states with lower energy.[29] From these results, we speculate that the slow re-ordered stage (the 2nd stage) in the blend film may facilitate better phase separation, while too strong interaction between the solvent and donor/acceptor materials leads to an undesirable phase separation, which can seriously affect the photovoltaic properties in the blend film.

To investigate the crystallization and phase separation in the blend film treated with different solvents, grazing incidence wide/small-angle X-ray scattering (GIWAXS/GISAXS) techniques were employed. The GIWAXS patterns and corresponding scattering profiles obtained along the out-of-plane (OOP) direction of the blend and neat films were displayed in **Figure 4**a–e, and Figure S3 (Supporting Information). From the GIWAXS patterns of the T6 neat film, shown in Figure S3b,e, (Supporting Information) it can be learned that the peak of $q \approx 3.3\ \text{nm}^{-1}$ corresponds to T6 and is referred to as the (100) peak. In Figure 4e, a sharper (100) peak is observed in the CB-treated film, which indicates a more ordered and compact molecular arrangement of T6. By fitting the π-π stacking peak ((010) peak). It can provide structure information on the small molecule N3 by fitting the π-π stacking peak ((010) peak). The use of a pole figure allows for the quantification of the percentage of edge-on and face-on crystallites.[30–31] The peaks observed near $\chi = 90°$ (vertical cut) and $\chi = 180°$ (horizontal cut) are attributed to the face-on and edge-on crystallites, respectively. As depicted in Figure 4f and Table S3 (Supporting Information), the area ratio of the two peaks ($\chi = 90°$–$135°$ and $\chi = 135°$–$180°$) is ≈7:3 in all blend films, which implies a majority face-on orientation. Specifically, the percentage of face-on orientation in the FB, CB, BB, and IB-treated films is 77.55%, 66.35%, 65.96%, and 70.52%, respectively. As reported in the literature,[32–33] the presence of a mixed face-on and edge-on orientation facilitates the formation of 3D charge pathways, promoting efficient charge transport. The position and full width at half maximum (FWHM) values of the (100) and (010) peaks are summarized in Table S4 (Supporting Information). The crystal coherence length (*CCL*) can be calculated using the Scherrer equation, which considers the crystallite size to be equal to the CCL.[34] Here, we can quantitatively assess the degree of crystallization of T6 and N3 in the blend film under different SVA conditions. The crystal coherence length (CCL) of the (010) peak in the FB, CB, BB, and IB-treated films is measured to be 5.04, 4.38, 4.39, and 4.55 nm, respectively. Except for the FB-treated films, all other solvent-treated films exhibit similar levels of crystallization. Previous literature has reported that excessively large crystallinity may hinder the effective dissociation of excitons, which could explain the lower power conversion efficiency (PCE) observed in the FB-treated ASM-OSC

© 2023 Wiley-VCH GmbH

16146840, 0, Downloaded from https://onlinelibrary.wiley.com/doi/10.1002/aenm.202302731 by Shenzhen Polytechnic, Wiley Online Library on [22/11/2023]. See the Terms and Conditions (https://onlinelibrary.wiley.com/terms-and-conditions) on Wiley Online Library for rules of use; OA articles are governed by the applicable Creative Commons License

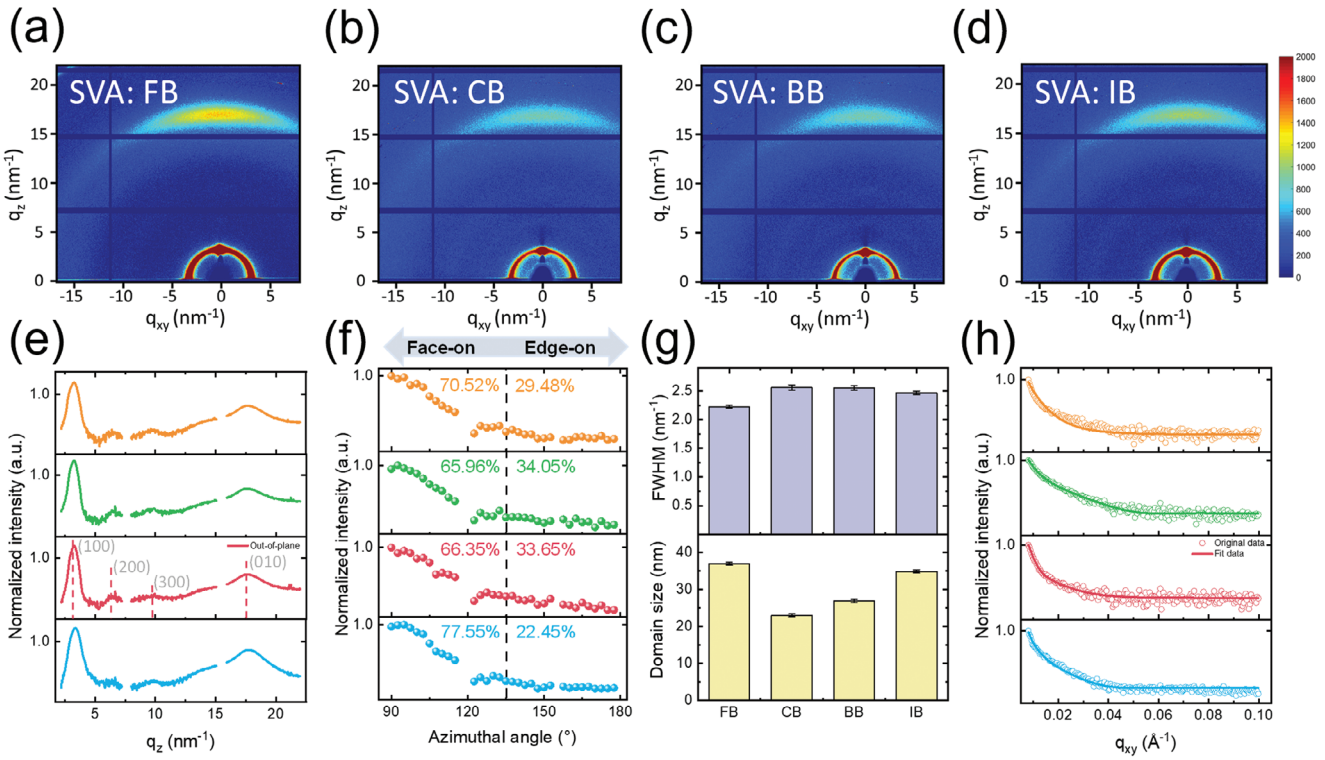

Figure 4. a–d) 2D GIWAXS patterns of T6: N3 films with various SVA solvents. e) OOP scattering profiles (from bottom to top: FB, CB, BB, and IB, respectively) from GIWAXS patterns. f) The intensity-corrected pole figures of the (010) peak. g) The FWHM of (010) peak on the OOP direction, and the domain size obtained by fitting h) IP scattering profiles from GISAXS patterns.

devices.[35] At the mesoscale level, we conducted GISAXS measurements to further investigate the nanoscale phase separation behavior. The scattering profiles along the defined region were obtained from Figure S4 (Supporting Information) and plotted in Figure 4h. To quantify and compare the phase separation in the solvent-treated film, the scattering profiles were fitted with a universal model based on the effective interface approximation of the distorted wave Born approximation (DWBA).[36] The domain size of the amorphous phase (ξ) in the films treated with FB, CB, IB, and BB was calculated to be 37.0, 23.0, 26.9, and 34.9 nm, respectively. It indicates a better phase separation in the CB-treated film, which may be more comparable to the theoretical exciton diffusion length. In contrast, the domain size in the FB and IB-treated films appears to be too large, indicative of higher aggregation. This observation aligns with the results of UV–vis absorption and morphology analysis. Based on these results, we speculate that the CB-treated film with a gradual re-ordered stage achieves an appropriate crystallinity and phase separation, thereby enabling efficient charge separation and transport. Conversely, the robust interaction between the FB and the blend film leads to an excessive crystallinity and oversized aggregation, which will impede the exciton dissociation in the blend film.

To further verify the effects of domain size and crystallinity changes on photovoltaic performance, we prepared devices with FB, CB, BB, and IB treated thin films, respectively. The device structure used for optimization was ITO/PEDOT:PSS/T6:N3/phen-NaDPO/Ag. The current density–voltage (J–V) curves and corresponding parameters for the best device performance achieved by different solvents are shown in **Figure 5**a and **Table 1** (More detailed data can be found in Table S5, Supporting Information). After data analysis, we found that the devices treated with FB exhibit a relatively low PCE of 14.8%, with a V_{OC} of 0.843 V, a J_{SC} of 25.72 mA cm^{-2}, and a low *FF* of 69.1%. However, devices treated with BB and IB showed relatively improved PCE values of 15.3% and 15.2%, respectively. Interestingly, the CB-treated device exhibits a remarkable PCE of 16.2% with an improved V_{OC} of 0.846 V and *FF* of 74.3%. This further indicates the importance of small and continuous domain size structures for achieving high-performance ASM-OSCs. The integral current densities were calculated as 24.50, 24.61, 24.68, and 24.70 mA cm^{-2} for FB, CB, BB, and IB, respectively, which are in agreement with the J_{SC} value obtained from the optimized devices within a 5% mismatch. By plotting the V_{OC} versus the logarithm of the J_{SC} as a function of light intensity, the slope of the resulting curve is proportional to the diode ideality factor (n).[37] As depicted in Figure 5c, the slopes of the V_{OC} as a function of ln(J_{SC}) increase as the light intensity decreases, particularly for devices treated with FB, which indicates that the blend film treated with the FB solvent suffers from the highest trap-assisted recombination. The impact of SVA solvents on the charge extraction and carrier recombination is further studied by transient photovoltage (TPV) and transient photocurrent (TPC). The carrier lifetime (τ lifetime) of FB, CB, BB, and IB-treated devices are 2.17, 2.36, 2.23, and 2.35 µs, respectively. The charge extraction time (τ extract) of FB, CB, BB, and

© 2023 Wiley-VCH GmbH

16146840, 0, Downloaded from https://onlinelibrary.wiley.com/doi/10.1002/aenm.202302731 by Shenzhen Polytechnic, Wiley Online Library on [22/11/2023]. See the Terms and Conditions (https://onlinelibrary.wiley.com/terms-and-conditions) on Wiley Online Library for rules of use; OA articles are governed by the applicable Creative Commons License

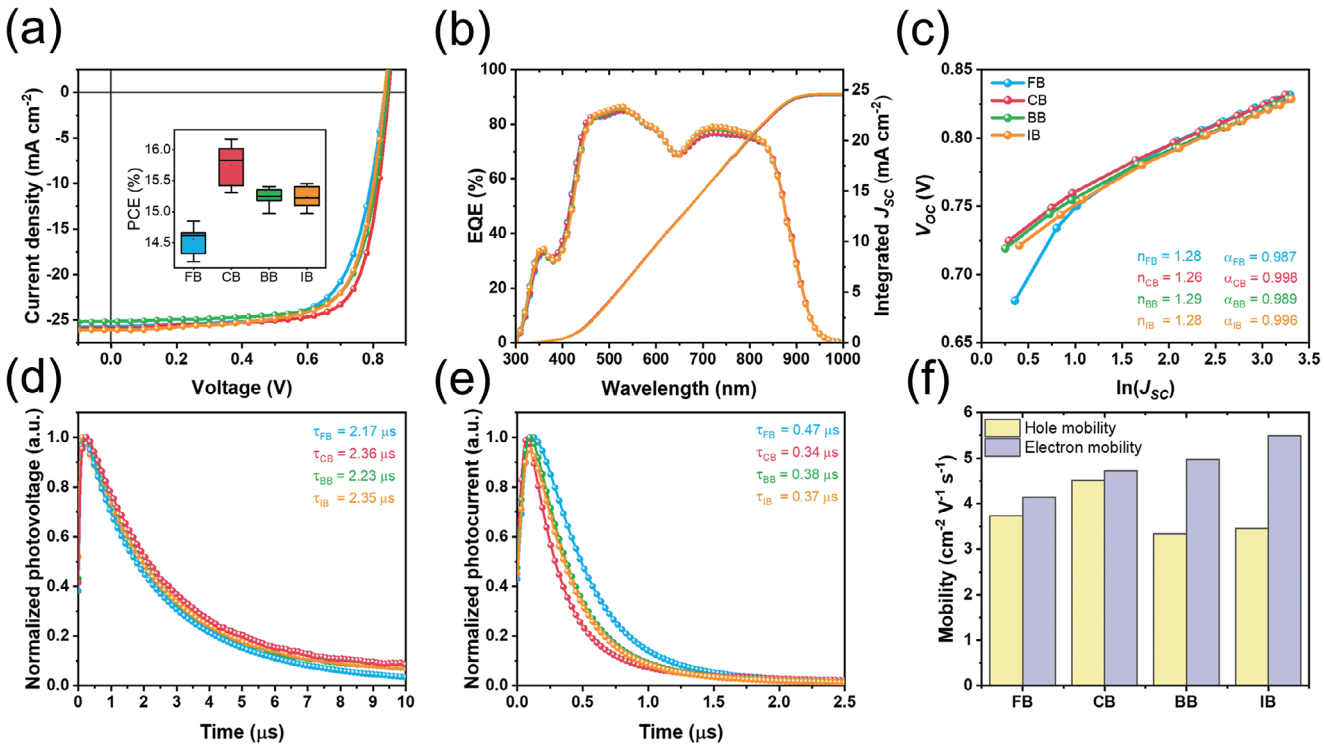

Figure 5. a) *J–V* curves of optimized ASM-OSC devices under different solvent conditions. b) The EQE curves of optimized ASM-OSC devices under different solvent conditions. c) Light intensity-dependent V_{OC} versus ln(J_{SC}) from 0.1 to 100 mW cm^{-2} under different solvent conditions. d) Transient photovoltage and e) transient photocurrent of optimized devices. f) Hole and electron mobilities of blend films under different solvents.

IB-treated devices are 0.47, 0.34, 0.38, and 0.37 µs, respectively. The longest τ lifetime of 2.36 µs and the shortest τ extract of 0.34 µs are simultaneously achieved in the CB-treated ASM-OSC device, which corresponds to an improvement in charge carrier compounding and extraction via effective molecular aggregation and morphology control. In order to elucidate the impact of different SVA solvents on charge transport processes, the mobilities of both hole and electron carriers were estimated using the space-charge-limited current (SCLC) model.[38–40] The hole mobility μ_h and electron mobility μ_e are displayed in Figure 5f and Table S6 (Supporting Information). The μ_h and μ_e of FB, CB, BB, and IB-treated devices were 3.73/4.14, 4.51/4.72, 3.34/4.97, and 3.46/5.49 × 10^{-4} cm^2 V^{-1} S^{-1}, respectively. It was observed that the CB-treated blend films had relatively high hole mobility, which played a positive role in promoting the balance of electron mobility, and the most balanced μ_e/μ_h value of 1.05. This balanced mobility ratio facilitates an improvement in the *FF* and PCE.[22]

3. Conclusion

In summary, we conducted a systematic study on the relationship between domain size structure regulation and photovoltaic performance of ASM-OSCs using a comprehensive set of characterization methods. We employed in situ UV–vis spectroscopy to enhance our comprehension of the evolution characteristics of the domain size structure of T6:N3 thin films under SVA treatment. During the SVA process, as the solvent permeates the film, small molecules transition from a high-energy disordered configuration to a significantly ordered state within this solid/liquid-like film through movement and translation. Furthermore, our research results demonstrate that the slow reordered stage in the blend film facilitates better phase separation and proper grain size, while too strong interaction between the solvent and donor/acceptor materials leads to large grains and undesirable phase separation, which can seriously affect the photovoltaic properties in the blend film. A continuous and uniform

Table 1. Photovoltaic parameters of ASM-OSCs annealing with different solvents.

Solvent	V_{OC} [V]	J_{SC} [mA cm^{-2}]	*FF* [%]	PCE [Average[a)]]	J_{SC}^{cal}[mA cm^{-2}]
FB	0.834 (0.834±0.004)	25.72 (25.43±0.75)	69.1 (69.4±1.5)	14.8 (14.7±0.2)	24.50
CB	0.846 (0.842±0.006)	25.81 (25.78±0.61)	74.3 (72.5±0.7)	16.2 (15.8±0.3)	24.61
BB	0.836 (0.835±0.005)	25.82 (25.70±0.39)	70.7 (70.6±1.2)	15.3 (15.2±0.2)	24.68
IB	0.834 (0.831±0.005)	25.91 (25.91±0.36)	69.9 (70.6±1.2)	15.2 (15.2±0.2)	24.70

[a)] Average PCE and deviation values were calculated over 15 devices.

© 2023 Wiley-VCH GmbH

16146840, 0, Downloaded from https://onlinelibrary.wiley.com/doi/10.1002/aenm.202302731 by Shenzhen Polytechnic, Wiley Online Library on [22/11/2023]. See the Terms and Conditions (https://onlinelibrary.wiley.com/terms-and-conditions) on Wiley Online Library for rules of use; OA articles are governed by the applicable Creative Commons License

domain size structure can enhance the performance of ASM-OSCs by achieving favorable phase separation and reducing recombination. Ultimately, ASM-OSC devices based on CB-treated demonstrated an impressive PCE of 16.2%, outperforming the efficiencies of FB-treated (14.8%), BB-treated (15.3%), and IB-treated (15.2%) devices. These outcomes underscore the significance of domain size regulation and morphology control as pivotal approaches in advancing ASM-OSCs.

Supporting Information

Supporting Information is available from the Wiley Online Library or from the author.

Acknowledgements

H.H. thanks the support from Scientific Research Startup Fund for Shenzhen High-Caliber Personnel of Shenzhen Polytechnic (No. 6022310038k), the National Natural Science Foundation of China (No. 62004129), Shenzhen Science and Technology Innovation Commission (Project No. 20220811205532001), Guangdong Basic and Applied Basic Research Foundation (No. 2023A1515011677) and Innovation Team Project of Guangdong (2022KCXTD055). J.L. thanks the support from China Postdoctoral Science Foundation (2022M720156), and the Post-Doctoral Foundation Project of Shenzhen Polytechnic 6022331001K. C.Y. thanks the support from the National Natural Science Foundation of China (12175295, U1932118), the National Key R&D Program of China (No. 2021YFA1601004). G.L. thanks the support from Research Grants Council of Hong Kong (GRF grant 15221320, CRF C5037-18G, C7018-20G), the Hong Kong Polytechnic University funds (Sir Sze-yuen Chung Endowed Professorship Fund (8-8480), and RISE (Q-CDA5).

Conflict of Interest

The authors declare no conflict of interest.

Author Contributions

X.S. and J.L. contributed equally to this work. X.S., J.L., and H.H. performed conceptualization. X.S. performed methodology and critical data curation. X.S. and J.L. wrote original draft. X.S., J.L., and H.H. reviewed and edited the manuscript. F.W., C.Z., and C.Y. performed in situ UV–vis absorption and GIWAX test. X.Z. and G.Z. performed the TPV and TPC tests. T.X. provided material of acceptor source. H.L. performed other data curation. C.Y., G.L., and H.H.performed supervision.

Data Availability Statement

Research data are not shared.

Keywords

all small molecules, in situ UV–vis spectroscopy, organic solar cells, phase separation

Received: August 18, 2023
Revised: October 23, 2023
Published online:

[1] Z. Luo, Y. Gao, H. Lai, Y. Li, Z. Wu, Z. Chen, R. Sun, J. Ren, C.'e Zhang, F. He, H. Woo, J. Min, C. Yang, *Energy Environ. Sci.* **2022**, *15*, 4601.
[2] J. Wu, M. Gao, Y. Chai, P. Liu, B. Zhang, J. Liu, L. Ye, *Mater. Rep.: Energy* **2021**, *1*, 100062.
[3] T.-P. Huynh, H. Haick, *Adv. Mater.* **2018**, *30*, 1802337.
[4] D. Wang, H. Liu, Y. Li, G. Zhou, L. Zhan, H. Zhu, X. Lu, H. Chen, C.-Z. Li, *Joule* **2021**, *5*, 945.
[5] L. Zhu, M. Zhang, J. Xu, C. Li, J. Yan, G. Zhou, W. Zhong, T. Hao, J. Song, X. Xue, Z. Zhou, R. Zeng, H. Zhu, C.-C. Chen, R. C. I. Mackenzie, Y. Zou, J. Nelson, Y. Zhang, Y. Sun, F. Liu, *Nat. Mater.* **2022**, *21*, 656.
[6] Y. Cui, Y. Xu, H. Yao, P. Bi, L. Hong, J. Zhang, Y. Zu, T. Zhang, J. Qin, J. Ren, Z. Chen, C. He, X. Hao, Z. Wei, J. Hou, *Adv. Mater.* **2021**, *33*, 2102420.
[7] J. Fu, P. W. K. Fong, H. Liu, C.-S. Huang, X. Lu, S. Lu, M. Abdelsamie, T. Kodalle, C. M. Sutter-Fella, Y. Yang, G. Li, *Nat. Commun.* **2023**, *14*, 1760.
[8] Q. Fan, R. Ma, Z. Bi, X. Liao, B. Wu, S. Zhang, W. Su, J. Fang, C. Zhao, C. Yan, K. Chen, Y. Li, C. Gao, G. Li, W. Ma, *Adv. Funct. Mater.* **2023**, *33*, 2211385.
[9] J. Wang, Y. Wang, P. Bi, Z. Chen, J. Qiao, J. Li, W. Wang, Z. Zheng, S. Zhang, X. Hao, J. Hou, *Adv. Mater.* **2023**, *35*, 2301583.
[10] Y. Sun, L. Nian, Y. Kan, Y. Ren, Z. Chen, L. Zhu, M. Zhang, H. Yin, H. Xu, J. Li, X. Hao, F. Liu, K. Gao, Y. Li, *Joule* **2022**, *6*, 2835.
[11] Y. Gao, X. Yang, W. Wang, R. Sun, J. Cui, Y. Fu, K. Li, M. Zhang, C. Liu, H. Zhu, X. Lu, J. Min, *Adv. Mater.* **2023**, *35*, 2300531.
[12] H. Tang, C. Yan, J. Huang, Z. Kan, Z. Xiao, K. Sun, G. Li, S. Lu, *Matter* **2020**, *3*, 1403.
[13] R. Zhou, Z. Jiang, C. Yang, J. Yu, J. Feng, M. A. Adil, D. Deng, W. Zou, J. Zhang, K. Lu, W. Ma, F. Gao, Z. Wei, *Nat. Commun.* **2019**, *10*, 5393.
[14] L. Zhang, X. Zhu, D. Deng, Z. Wang, Z. Zhang, Y. Li, J. Zhang, K. Lv, L. Liu, X. Zhang, H. Zhou, H. Ade, Z. Wei, *Adv. Mater.* **2022**, *34*, 2106316.
[15] T. Xu, J. Lv, K. Yang, Y. He, Q. Yang, H. Chen, Q. Chen, Z. Liao, Z. Kan, T. Duan, K. Sun, J. Ouyang, S. Lu, *Energy Environ. Sci.* **2021**, *14*, 5366.
[16] L. Nian, Y. Kan, K. Gao, M. Zhang, N. Li, G. Zhou, S. B. Jo, X. Shi, F. Lin, Q. Rong, F. Liu, G. Zhou, A. K.-Y. Jen, *Joule* **2020**, *4*, 2223.
[17] Z. Li, X. Wang, N. Zheng, A. Saparbaev, J. Zhang, C. Xiao, S. Lei, X. Zheng, M. Zhang, Y. Li, B. Xiao, R. Yang, *Energy Environ. Sci.* **2022**, *15*, 4338.
[18] J. Ge, L. Hong, H. Ma, Q. Ye, Y. Chen, L. Xie, W. Song, D. Li, Z. Chen, K. Yu, J. Zhang, Z. Wei, F. Huang, Z. Ge, *Adv. Mater.* **2022**, *34*, 2202752.
[19] J. Qin, Z. Chen, P. Bi, Y. Yang, J. Zhang, Z. Huang, Z. Wei, C. An, H. Yao, X. Hao, T. Zhang, Y. Cui, L. Hong, C. Liu, Y. Zu, C. He, J. Hou, *Energy Environ. Sci.* **2021**, *14*, 5903.
[20] D. Hu, Q. Yang, H. Chen, F. Wobben, V. M. Le Corre, R. Singh, T. Liu, R. Ma, H. Tang, L. J. A. Koster, T. Duan, H. Yan, Z. Kan, Z. Xiao, S. Lu, *Energy Environ. Sci.* **2020**, *13*, 2134.
[21] T. Xu, J. Lv, Z. Chen, Z. Luo, G. Zhang, H. Liu, H. Huang, D. Hu, X. Lu, S. Lu, C. Yang, *Adv. Funct. Mater.* **2023**, *33*, 2210549.
[22] J. Ge, L. Hong, W. Song, L. Xie, J. Zhang, Z. Chen, K. Yu, R. Peng, X. Zhang, Z. Ge, *Adv. Energy Mater.* **2021**, *11*, 2100800.
[23] K. Sun, Z. Xiao, E. Hanssen, M. F. G. Klein, H. H. Dam, M. Pfaff, D. Gerthsen, W. W. H. Wong, D. J. Jones, *J. Mater. Chem. A* **2014**, *2*, 9048.
[24] B. Walker, A. Tamayo, D. T. Duong, X.-D. Dang, C. Kim, J. Granstrom, T.-Q. Nguyen, *Adv. Energy Mater.* **2011**, *1*, 221.
[25] Y. Wang, Z. Liang, X. Liang, X. Wen, Z. Cai, Z. Shao, J. Zhang, Y. Ran, L. Yan, G. Lu, F. Huang, L. Hou, *Adv. Energy Mater.* **2023**, *13*, 2300524.
[26] L. Chen, J. Yi, R. Ma, L. Ding, T. A. Dela Peña, H. Liu, J. Chen, C. Zhang, C. Zhao, W. Lu, Q. Wei, B. Zhao, H. Hu, J. Wu, Z. Ma, X. Lu, M. Li, G. Zhang, G. Li, H. Yan, *Adv. Mater.* **2023**, *35*, 2301231.

© 2023 Wiley-VCH GmbH

16146840, 0, Downloaded from https://onlinelibrary.wiley.com/doi/10.1002/aenm.202302731 by Shenzhen Polytechnic, Wiley Online Library on [22/11/2023]. See the Terms and Conditions (https://onlinelibrary.wiley.com/terms-and-conditions) on Wiley Online Library for rules of use; OA articles are governed by the applicable Creative Commons License

[27] H. W. Ro, J. M. Downing, S. Engmann, A. A. Herzing, D. M. Delongchamp, L. J. Richter, S. Mukherjee, H. Ade, M. Abdelsamie, L. K. Jagadamma, A. Amassian, Y. Liu, H. Yan, *Energy Environ. Sci.* **2016**, *9*, 2835.
[28] R. Steyrleuthner, M. Schubert, I. Howard, B. Klaumünzer, K. Schilling, Z. Chen, P. Saalfrank, F. Laquai, A. Facchetti, D. Neher, *J. Am. Chem. Soc.* **2012**, *134*, 18303.
[29] J. Vogelsang, J. Brazard, T. Adachi, J. C. Bolinger, P. F. Barbara, *Angew. Chem., Int. Ed. Engl.* **2011**, *50*, 2257.
[30] G. Kim, S.-J. Kang, G. K. Dutta, Y.-K. Han, T. J. Shin, Y.-Y. Noh, C. Yang, *J. Am. Chem. Soc.* **2014**, *136*, 9477.
[31] J. Rivnay, R. Steyrleuthner, L. H. Jimison, A. Casadei, Z. Chen, M. F. Toney, A. Facchetti, D. Neher, A. Salleo, *Macromolecules* **2011**, *44*, 5246.
[32] T. Kumari, S. M. Lee, S.-H. Kang, S. Chen, C. Yang, *Energy Environ. Sci.* **2017**, *10*, 258.
[33] H. Bin, J. Yao, Y. Yang, I. Angunawela, C. Sun, L. Gao, L. Ye, B. Qiu, L. Xue, C. Zhu, C. Yang, Z.-G. Zhang, H. Ade, Y. Li, *Adv. Mater.* **2018**, *30*, 1706361.
[34] A. Mahmood, J.-L. Wang, *Sol. RRL* **2020**, *4*, 2000337.
[35] Y. Yue, B. Zheng, W. Yang, L. Huo, J. Wang, L. Jiang, *Adv. Mater.* **2022**, *34*, 2108508.
[36] P. Müller-Buschbaum, *Adv. Mater.* **2014**, *26*, 7692.
[37] T. Liu, Q. C. Burlingame, M. R. Ivancevic, X. Liu, J. Hu, B. P. Rand, Y.-L. Loo, *Adv. Energy Mater.* **2023**, *13*, 2300046.
[38] C. Zhang, J. Li, W. Deng, J. Dai, J. Yu, G. Lu, H. Hu, K. Wang, *Adv. Funct. Mater.* **2023**, *33*, 2301108.
[39] J. Lv, Q. Yang, W. Deng, H. Chen, M. Kumar, F. Zhao, S. Lu, H. Hu, Z. Kan, *Chem. Eng. J.* **2023**, *465*, 142822.
[40] Z. Peng, Y. Zhang, X. Sun, W. Zhao, F. Bian, Y. Geng, L. Ye, C. Yang, *Adv. Funct. Mater.* **2023**, *33*, 2213248.

© 2023 Wiley-VCH GmbH

16146840, 0, Downloaded from https://onlinelibrary.wiley.com/doi/10.1002/aenm.202302731 by Shenzhen Polytechnic, Wiley Online Library on [22/11/2023]. See the Terms and Conditions (https://onlinelibrary.wiley.com/terms-and-conditions) on Wiley Online Library for rules of use; OA articles are governed by the applicable Creative Commons License